Journal of Materials Chemistry A

ROYAL SOCIETY OF CHEMISTRY

PAPER

View Article Online
View Journal | View Issue

Cite this: *J. Mater. Chem. A*, 2025, **13**, 3379

Depolymerization of lignin into cycloalkanes over a hydrotalcite-derived NiFe alloy catalyst†

Hairui Jiao,[b] Yushuai Sang,[c] Hong Chen *[a] and Yongdan Li *[c]

Received 12th October 2024
Accepted 12th December 2024

DOI: 10.1039/d4ta07285e

rsc.li/materials-a

Herein, an $Ni_9Fe_1/NiAlO_z$ catalyst is reported to be an efficient catalyst for conversion of enzymatic hydrolysis lignin (EHL) and 2-phenethyl phenyl ether (PPE), a lignin dimer model compound. Interspecies electron transfer within the alloy phase enhances the intrinsic hydrogenation activity of Ni, while Fe doping generates abundant interfacial oxygen vacancies (OVs). The combination of H* from high-intensity hydrogen spillover and abundant OVs promotes the depolymerization of EHL into cycloalkanes. Because of this combination, $Ni_9Fe_1/NiAlO_z$ achieves 99.4% of PPE conversion under mild reaction conditions (100 °C, 0.8 MPa H_2, and 3 h) and achieves the yield of cycloalkanes (169.5 mg per g EHL at 300 °C) from EHL that exceeds the theoretical yield. The catalyst is also stable for 6 runs without much deactivation. This strategy provides new insights into the rational design of an efficient and stable transition metal catalyst using a simple preparation method for the valorization of EHL.

1 Introduction

Biomass is the most abundant renewable carbon resource of organic origin and the ideal feedstock for renewable fuel and value-added chemical production.[1,2] Lignin, the primary component of lignocellulose, is the only renewable feedstock for aromatic fuels and chemicals.[3] In recent years, there has been an increased interest in the depolymerization of lignin *via* C–O bond cleavage as a promising approach to derive valuable chemicals from natural and renewable resources.[4,5]

Lignin is a natural polymer made of benzene and propane-like units linked together with C–C and C–O bonds. Most aromatic monomers in lignin are connected *via* phenolic ether bonds (50–85%, depending on the plant species), such as β-O-4, α-O-4, and 4-O-5 bonds, with β-O-4 bonds being the most abundant.[6,7] The selective cleavage of the ether bond in lignin to yield monomers is particularly challenging. Given the complexity and variability of real lignin, model compounds have been intensively used in research to selectively cleave specific bonds in technical lignin.[8,9] Among the model compounds utilized, 2-phenethyl phenyl ether (PPE) is deemed suitable. Various types of Ni-catalysts have been reported for C–O bond cleavage. Chen *et al.*[10] used a defect-rich layered silicate-like nickel nanosheet catalyst for PPE conversion at 160 °C and 3 MPa H_2 and obtained 98.3% cycloalkanes and trace amounts of aromatic hydrocarbon products. Several studies have revealed that Ni metal alloys efficiently catalyze the transformation of lignin model molecules and facilitate C–O bond cleavage *via* hydrogenolysis. Mauriello *et al.*[11] achieved hydrogenolysis of PPE in isopropanol at 210 °C with a 3 wt% Pd/Ni catalyst and proposed that the synergy of palladium and nickel as alloys is crucial for enabling C–O bond scission and the subsequent formation of aromatic compounds. Chen *et al.*[12] designed a Ni_xLa_y/CNT (CNT, carbon nanotube) catalyst to achieve PPE C–O bond breaking at 240 °C, 4 h, and 2.0 MPa H_2 and observed that aryl groups played an important role in the competitive hydrogenation of phenol. Han *et al.*[13] obtained cyclohexanol and cyclohexane from phenol at 5 MPa H_2 and 250 °C using an NiFe alloy catalyst, demonstrating the synergy of Ni sites and Ni–Fe alloy sites in H_2 activation and C–O bond cleavage.

Layered double hydroxide (LDH), often called hydrotalcite-like compounds, and its derivatives are versatile materials with unique properties and wide variety of applications. The multiphase catalyst, a composite of metal nanoparticles and mixed metal oxides (MOs), obtained from LDH precursors has demonstrated excellent catalytic behavior.[14] Moreover, LDH-derived catalysts have shown considerable promise in lignin depolymerization reactions, achieving complete lignin liquefaction and high yields of monomers.[15,16] In addition, lignin-derived materials have been successfully utilized in advanced applications, such as strong bioadhesive hydrogels, conductive nanocapsules, and wearable bioelectrodes, showcasing the

[a]School of Environmental Science and Engineering, Tianjin University, Tianjin 300072, China. E-mail: chenhong_0405@tju.edu.cn

[b]Collaborative Innovation Center of Chemical Science and Engineering, Tianjin Key Laboratory of Applied Catalysis Science and Technology, State Key Laboratory of Chemical Engineering, School of Chemical Engineering, Tianjin University, Tianjin 300072, China

[c]Department of Chemical and Metallurgical Engineering, School of Chemical Engineering, Aalto University, Kemistintie 1, Espoo FI-00076, Finland. E-mail: yongdan.li@aalto.fi

† Electronic supplementary information (ESI) available. See DOI: https://doi.org/10.1039/d4ta07285e

potential of lignin-based materials in functional and biomedical fields.[17,18]

Herein, a co-precipitation technique is adopted for the preparation of highly active hydrotalcite-derived NiFe-based catalysts for the complete conversion of PPE and enzymatic hydrolysis lignin (EHL) to cycloalkanes. The incorporation of Fe species results in a catalyst with high oxygen affinity and an NiFe alloy with $Ni^{\delta-}$–$Fe^{\delta+}$, which exhibits excellent hydrodeoxygenation (HDO) and aromatic ring saturation performance.

2 Experimental

2.1 Catalyst preparation

All catalyst precursors were synthesized using a homogeneous co-precipitation technique with urea decomposition at 110 °C, as shown in Scheme 1. To prepare $Ni_9Fe_1/NiAlO_z$, 21.1 g $Ni(NO_3)_2{\cdot}6H_2O$ (99 wt%, Aladdin Co., Ltd), and 3.3 g $Fe(NO_3)_3{\cdot}9H_2O$ (99 wt%, Aladdin Co., Ltd) were dissolved in 75 mL deionized water with oxygen and CO_2 removed, followed by the addition of 9.2 g $Al(NO_3)_3{\cdot}9H_2O$ (98 wt%, Shanghai Macklin Biochemical Co., Ltd). After full dissolution, the liquid was denoted as solution A. Urea (42.2 g, 99 wt%, Shanghai Macklin Biochemical Co., Ltd) was dissolved in 50 mL deionized water and added to solution A, resulting in solution B. Solution B was transferred to a round bottom flask and stirred at 120 °C for 12 h under reflux. Subsequently, the slurry was aged for 12 h at 25 °C, and the resulting powder obtained *via* filtration, with a Ni to Fe ratio of 8 : 2, was roasted for 12 h at 500 °C in a muffle oven to obtain the catalyst precursor, denoted as $Ni_9Fe_1AlO_z$. Before the experiment, the $Ni_9Fe_1AlO_z$ catalyst was reduced at 460 °C for 3 h in 5 vol% H_2/Ar to obtain $Ni_9Fe_1/NiAlO_z$. The catalyst samples $Ni/NiAlO_z$, Fe/AlO_z, $Ni_9Fe_{0.5}/NiAlO_z$ and $Ni_9Fe_{1.5}/NiAlO_z$ were synthesized using a similar technique. In this context, $Ni_xFe_y/NiAlO_z$ refers to all the catalyst samples.

2.2 Catalyst characterization

X-ray diffraction (XRD) patterns were recorded at 10–80° at an 8° min^{-1} scanning rate using an X-pert powder diffractometer (Smartlab, Rigaku Corp., Japan). X-ray absorption fine structure (XAFS) K-edge spectra for Ni and Fe were collected using a table XAFS-500-A instrument from Anhui Chuangpu Instrument Technology Co. The elemental contents of Ni, Fe, and Al were determined using an inductively coupled plasma-optical emission spectroscopy (ICP-OES) instrument (model: 730-ES; Varian; Palo Alto, USA). 0.1 g of the sample was digested and subjected to the ICP test. The H_2-TPR was measured using an Altamira Instruments (AMI-300, USA) instrument and the catalyst was heated from 50 to 900 °C with a ramp of 10 °C min^{-1} under a flow of H_2/Ar, 5 vol% (v/v) at 30 mL min^{-1}, STP. The H_2-TPD tests of the samples were recorded using a MicrotracBEL (BELCAT-B, Japan) machine. Prior to the H_2-TPD test, pure H_2 was used for pretreatment at 300 °C for 0.5 h and maintained under a stream of He for 0.5 h. The sample was cooled to 100 °C and maintained with flowing H_2 (30 mL min^{-1}) for 0.5 h. The system was purged with inert gas at 100 °C until the baseline was stabilized. Finally, the temperature was ramped up to 800 °C at a rate of 10 °C min^{-1}. The WO_3 color change experiment was used to illustrate the hydrogen spillover of the catalyst. Photographs of samples (0.1 g) made with WO_3 (0.5 g) were mixed with the catalysts before treatment (0 s) and after treatment with 5% H_2/Ar at 180 °C for 30 s and 180 s. The thermogravimetric (TG) curves were measured using an STA449 F3 analyzer (PerkinElmer Diamond, USA) in an air stream, 50 mL min^{-1}, STP, and a temperature range of 50–800 °C at a heating rate of 5 °C min^{-1}. *In situ* FT-IR measurements of the PPE hydrogenation reaction were performed with the mixture of catalyst and PPE dried at 40 °C in a vacuum for 12 h. The sample was heated up to 100 °C under a flow of H_2 and kept for 3 h, and the spectra during the reaction were collected with a fixed time interval. The Raman spectra of the samples were obtained using a spectrometer, Horiba LabRAM HR Evolution, France, equipped with a DXR microscope at an excitation wavelength of 532 nm as the light source and a scan range of 1400–1700 cm^{-1}.

High-performance X-ray photoelectron spectroscopy (XPS) was used to reveal the valence states of the elements on the catalyst surface using a VG Scientific ESCALAB 250 spectrometer (Waltham, Massachusetts, USA). The morphology and structure of the samples were observed using a scanning electron microscope (SEM, S-4800, JEOL) and a transmission electron microscope (TEM, JEM-2100F, Hitachi). The sample microstructure and elemental distribution were also determined using the above two instruments. A Nicolet iS10 FTIR spectrometer (ThermoFisher Scientific Inc., UK) was used to measure the CO adsorption on the catalyst surface. The sample was heated to 200 °C and maintained for 1 h under a He atmosphere, 60 mL per min (STP), and then cooled to 30 °C to start recording the background. After that, a 30 min of CO adsorption was performed (1 vol% CO–He, 60 mL min^{-1}, STP), with one reading every 3 min. Finally, the CO desorption was done with a 30 minute He gas purge and 15 minutes of data collection. Two-dimensional heteronuclear single quantum coherence-nuclear magnetic resonance (2D-HSQC NMR) was obtained using a Bruker 600 MHz Avance III spectrometer. A 40 mg sample was dissolved in 0.5 mL dimethyl sulfoxide (DMSO) and tested after being completely dissolved. The ^1H resonance frequency was 600 MHz, and ^{13}C was 150.91 MHz.

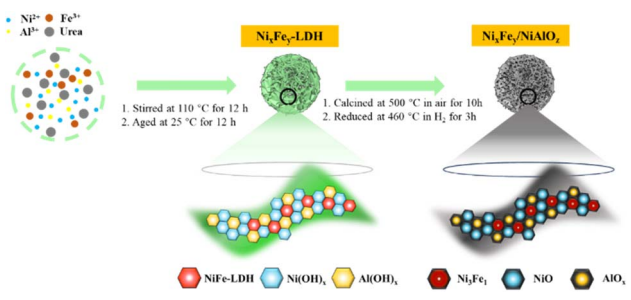

Scheme 1 Synthesis scheme for $Ni_xFe_y/NiAlO_z$.

2.3 Lignin model compound and EHL conversion

500 mg dimers (PPE and 4,4′-dihydroxydiphenylmethane, 98.0%, Tianjin Heowns Biochem Technologies; diphenyl ether

and biphenyl, 99.0%, Shanghai Aladdin Biochemical Technology Co., Ltd) or 500 mg EHL, 500 mg catalyst, and 70 mL *n*-dodecane (99.0%, Shanghai Dibai Biotechnology Co., Ltd) as solvent were mixed in an autoclave (Anhui Kemi Instrument Co., Ltd). There was no catalyst in the blank reaction, and the other conditions were retained. After sealing and purging, the reactor was charged with the prescribed H_2 pressure and heated to a certain temperature, 60–300 °C, under 550 rpm stirring for a certain time, 0–10 h; thereafter, the reactor was cooled to room temperature. Subsequently, the reaction mixture was collected and mixed with the solution obtained by washing the autoclave with dodecane. An internal standard, 70 mg trimethylbenzene, was added. In the cycling experiments, the isolated catalyst was washed with ethanol, dried in a vacuum oven at 60 °C for 2 h, and used in the next reaction without the addition of a new catalyst. After recovery, the catalyst samples were marked as P–$Ni_9Fe_1/NiAlO_z$ after the sixth cycle reaction with PPE.

The analysis of liquid products was carried out using the same equipment and method reported previously.[17] The liquid products were identified and quantified using a gas chromatograph-mass (GC-MS) spectrometer and a gas chromatograph equipped with a flame ionization detector (GC-FID), respectively. The gaseous products were qualitatively analyzed using a Hiden Analytical HPR20 mass spectrometer.

PPE conversion and product yield were calculated using eqn (1) and (2) (monomer), and (3) (dimer). Moreover, the conversion and yield for EHL are calculated according to eqn (4) and (5).

$$\text{PPE conversion} = 1 - \frac{\text{the mole of the remaining substrate}}{\text{the mole of the initial substrate}}, \quad (1)$$

$$\text{Monomer selectivity} = \frac{\text{the mole of monomer product}/2}{\text{the mole of lignin model compound}} \times 100\%, \quad (2)$$

$$\text{Dimer selectivity} = \frac{\text{the mole of dimer product}}{\text{the mole of the lignin model compound}} \times 100\%, \quad (3)$$

$$\text{EHL conversion} = 1 - \frac{\text{mass weight}_{\text{solid residue}} - \text{mass weight}_{\text{recovered catalyst}}}{\text{mass weight}_{\text{initial EHL}}}, \quad (4)$$

$$\text{Total yield (mg per g EHL)} = \frac{\text{sum of the mass weight of each product}}{\text{the mass of raw lignin}} \times 100\%. \quad (5)$$

3 Results

3.1 Catalytic activity

3.1.1 PPE hydrogenation activity. The catalytic performance of the catalyst samples for the PPE hydrogenation reaction (100 °C, 0.8 MPa H_2, 3 h) is shown in Table 1. The blank experiment and the experiment with Fe/AlO_z as a catalyst exhibit no conversion. The reaction with Ni/$NiAlO_z$ (entry 2) resulted in PPE conversion of 21.3, and the product contains 4.1% ethylbenzene, 6.1% ethylcyclohexane, 10.3% cyclohexanol, and 0.8% cyclohexane. For the samples with both Ni and Fe, with an increase in the Fe content, a volcano-shaped curve is observed for PPE conversion, with $Ni_9Fe_1/NiAlO_z$ giving the highest PPE conversion of 99.4%. The conversions of $Ni_9Fe_{0.5}/NiAlO_z$ and $Ni_9Fe_{1.5}/NiAlO_z$ are 92.6 and 63.2%, respectively. The reaction products using $Ni_9Fe_y/NiAlO_z$ as catalysts contain similar molecules, cyclohexanol (37.6, 48.0, and 26.4%), ethylcyclohexane (30.8, 49.3, and 25.2%), ethylbenzene (20.8, 0, and 10.2%), and cyclohexane (2.1, 2.1, and 1.4%, respectively). The selectivity trend of the three Ni–Fe containing catalyst samples indicates that the $Ni_9Fe_1/NiAlO_z$ sample possesses the highest hydrogenation activity, evidenced by the lowest ethylbenzene yield. In the products of all the three catalyst samples, no phenolic products are detected, meaning that all the three samples are very good hydrogenation catalysts.

The results of the PPE hydrogenation reaction in different solvents and with or without hydrogen pressure are presented in Table S1.† In the absence of externally supplied hydrogen, the reaction with alcohol solvents and water did not proceed, indicating that the hydrogen supply is crucial for low-temperature hydrogenation. As displayed by the data in Table S1,† when hydrogen pressure was applied, the reaction occurred, but PPE conversion was significantly lower than that in the reaction in *n*-dodecane, decreasing to 33.4% in isopropanol, 19.8% in ethanol, 10.1% in methanol, and 8.5% in water.

Fig. 1 illustrates the significant variation in product selectivity during the hydrogenation of PPE over time. Initially, at 0 min, no products are observed, indicating that the reaction has not yet begun. At 30 min, the conversion reaches 7.8%, with phenol (4%) and ethylbenzene (3.8%) as the primary products, while cyclohexanol and cyclohexanone are absent. At 60 min, conversion increases to 14.4%, with cyclohexanone (0.5%), phenol (6.9%), and ethylbenzene (7%) detected, marking the onset of phenyl group hydrogenation. By 90 min, conversion increases to 39.8%, yielding cyclohexanol (8.3%), phenol (10.6%), ethylbenzene (19.7%), and cyclohexanone (1.2%), suggesting an accelerated formation of cyclohexanol. At 120 min, conversion reaches 52.1%, with cyclohexanol (9%), phenol (15.3%), and ethylbenzene (27.8%) as major products, while cyclohexanone remains negligible. At 150 min, conversion climbs to 62.8%, accompanied by a shift toward saturated intermediates, with cyclohexanol (10.9%), phenol (17.5%), ethylbenzene (33.2%), and ethylcyclohexane (1.2%) detected. At 180 min, conversion further increases to 82.4%, with cyclohexanol (40.1%) dominating, phenol decreasing to 3.2%, and ethylbenzene at 35.1%, along with trace amounts of ethylcyclohexane. At 210 min, conversion reaches 96.8%, with cyclohexanol (51.4%) and ethylcyclohexane (20.9%) as the major products, while ethylbenzene decreases to 24.5%. Finally, between 240 and 300 min, conversion stabilizes at ~99%, with cyclohexanol (50.3–50.5%) and ethylcyclohexane (48.4%)

Table 1 Results of PPE conversion reactions involving different catalysts. Reaction conditions: 500 mg catalyst, 500 mg PPE, 70 mL *n*-dodecane, 100 °C, 3 h, and 0.8 MPa H_2 pressure

Catalysts	Conv. (%)	Selec. (%)			
		Cyclohexane	Cyclohexanol	Ethylbenzene	Ethylcyclohexane
Fe/AlO_x	—	—	—	—	—
$Ni/NiAlO_x$	21.3	0.8	10.3	4.1	6.1
$Ni_9Fe_{0.5}/NiAlO_x$	91.3	2.1	37.6	20.8	30.8
$Ni_9Fe_1/NiAlO_x$	99.4	2.1	48.0	—	49.3
$Ni_9Fe_{1.5}/NiAlO_x$	63.2	1.4	26.4	10.2	25.2
Blank	—	—	—	—	—

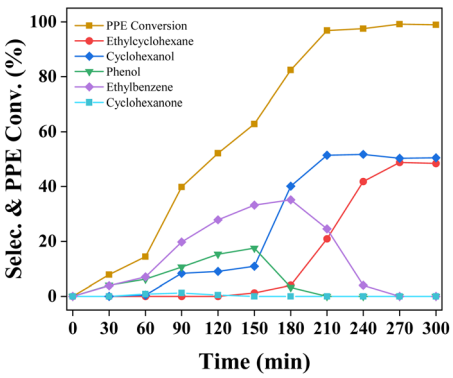

Fig. 1 Selectivity of reaction products for the $Ni_9Fe_1/NiAlO_z$ catalyst with PPE at various conversion levels. Reaction conditions: 200 mg catalyst, 500 mg PPE, 70 mL *n*-dodecane, 100 °C, and 0.8 MPa H_2 pressure.

dominating, while phenol and ethylbenzene are no longer detected, indicating complete saturation of the aromatic substrate.

3.1.2 Effect of reaction conditions. The effect of temperature on the PPE conversion and product selectivity with sample $Ni_9Fe_1/NiAlO_z$ as a catalyst is shown in Fig. 2a. The reaction does not occur at 60 °C. At 80 °C, the conversion is 27.1%. The product contains 2.3% ethylcyclohexane, 12.7% ethylbenzene and 11.1% cyclohexanol. When the reaction temperature is 100 °C, PPE conversion reaches 99.4% and the major products are 49.3% ethylcyclohexane and 48.0% cyclohexanol. At 140 °C, the conversion attains 99.6%. The product contains 49.6% ethylcyclohexane, 33.3% cyclohexanol and 16.7% cyclohexane. At 300 °C, the conversion becomes 99.5% and the product contains 49.4% ethylcyclohexane and 50.1% cyclohexane. As the temperature increases, cyclohexanol disappears and the content of cyclohexane increases.

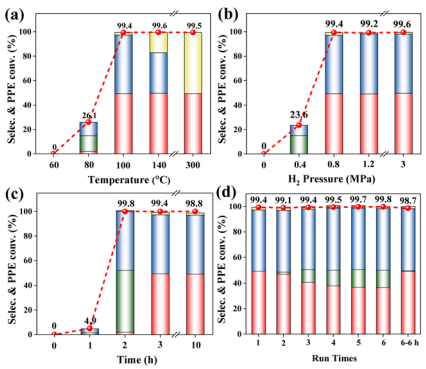

Fig. 2 Influences of (a) reaction temperature, (b) H_2 pressure and (c) reaction time on the HDO of PPE. The catalytic results for (d) PPE over $Ni_9Fe_1/NiAlO_z$ catalyst. Reaction conditions: 500 mg catalyst, 500 mg PPE, 70 mL *n*-dodecane, 100 °C, 3 h, and 0.8 MPa H_2 pressure.

The H_2 pressure effects are illustrated in Fig. 2b. Without hydrogen input, conversion does not occur. When the H_2 pressure is 0.4 MPa, the PPE conversion is 23.6% and the product contains 8.4% cyclohexanol and 15.2% ethylbenzene. At 0.8 MPa H_2, PPE conversion is 99.4% and the product has 48.0% cyclohexanol, 49.3% ethylcyclohexane, and 2.1% cyclohexane. Further increasing the H_2 pressure to 1.2 and 3 MPa resulted in negligible changes in conversion and product selectivity, suggesting that an increase in H_2 pressure does not lead to PPE hydrogenation and deep hydrogenation of the products.

The effect of the reaction time is plotted in Fig. 2c. During the first 1 h, only 4.9% PPE is converted, and the product contains cyclohexanol and ethylbenzene. At 2 h, the conversion increases drastically to 99.8%, with selectivity to 50.2% ethylbenzene, 48.0% cyclohexanol and 0.6% cyclohexane. At 3 h, the conversion is 99.4%, and the product has 49.3% ethyl cyclohexane, 48.0% cyclohexanol and 2.1% cyclohexane. When the reaction time is extended to 10 h, the conversion is measured as 99.8%, and the composition of the product is similar to that measured at 3 h. At this 100 °C temperature, the yield of cyclohexanol is stabilized, *i.e.* no deeper hydrogenation.

3.1.3 Catalyst recyclability. In Fig. 2d, the stability of the $Ni_9Fe_1/NiAlO_z$ catalyst under optimized conditions is illustrated with PPE as the reactant under the conditions of 100 °C, 3 h, and 0.8 MPa H_2. After each run, the conversion and cyclohexanol yield remain constant with a gradual increase in ethylbenzene yield. The second and third runs have the same conversion, but the selectivity of ethylbenzene is increased and kept unchanged in the subsequent 5–6 runs. At the end of the sixth run, the ethylbenzene yield is 13.3%, in comparison to the fourth run (12.1%) and fifth run (13.6%). The yield of ethylbenzene increased and then remained unchanged, indicating that the hydrogenation activity of the catalyst slightly decreased with an increase in the number of runs. A parallel sample

underwent six similar runs. For the six runs, the reaction time was extended to 6 h, and the product composition obtained was very close to that of the first one, with two major products, cyclohexanol and ethylcyclohexane.

3.1.4 Dimer conversion. To further support the high hydrogenation activity, additional dimer reactions were conducted using $Ni_9Fe_1/NiAlO_z$ catalyst (Fig. 3). A set of dimer compounds, namely diphenyl ether, 4,4′-dihydroxydiphenylmethane, and biphenyl, were used in this study. The diverse activity patterns of the catalysts in various reactions, such as hydrogenation of aromatic rings, C–O bond hydrogenolysis, and C–C bond hydrogenolysis, were analyzed. In the reaction of diphenyl ethers, three products, namely cyclohexane (32.1%), cyclohexanol (26.4%), and cyclohexyloxy-cyclohexane (41.5%), are observed at 100 °C (Fig. 3a). The percentage of bond-breaking hydrogenation products gradually increases with increasing temperature, yielding only cyclohexane at 220 °C. Adsorption of diphenyl ethers on the $Ni_9Fe_1/NiAlO_z$ catalyst is similar to that of PPE, with preferential scission of β-O-4 bonds in the PPE, while the catalyst undergoes predominant hydrogenation of aromatic rings owing to the superior bond dissociation energy of 4-O-5 linkages.

Moreover, the hydrogenation reactions of 4,4′-dihydroxydiphenylmethane and biphenyl at 100, 200, and 300 °C were carried out (Fig. 3b and c). With an increase in temperature, a gradual C–C bond cleavage occurs; however, the percentage of cleaved products is relatively low, indicating that the catalysts demonstrate high activity for the hydrogenation of aromatic rings. Further experiments were conducted with 4-phenylphenol, cyclohexyloxy-cyclohexane, phenylcyclohexane, and bicyclohexyl, and the results are shown in Fig. S1.† The conversion of 4-phenylphenol is only 13.4%, dominated by the hydrogenation product of the benzene ring; the hydroxyl group is not removed, and the C–C bond is not broken in this reaction. Partial bond-breaking products (7.8% cyclohexane) appear in the phenylcyclohexane reaction, while no C–O bond-breaking and C–C bond-breaking occur in the cyclohexyloxy-cyclohexane and bicyclohexyl reactions, respectively, which implies that when the benzene ring is fully hydrogenated, a further reaction does not occur, indicating low activity in cleaving $C_{aliphatic}$–$C_{aliphatic}$ bonds despite its bond dissociation energy. Additionally, the weaker aliphatic peak in the *in situ* FT-IR spectra confirms the significant role of adsorption on the catalyst surface in its activation.[19]

3.1.5 One-pot conversion of EHL. In Fig. 4a, EHL without catalytic reaction can give a total yield of 43.6 mg per g EHL monomers with a conversion of 56.2%. $Ni_9Fe_1/NiAlO_z$ catalyst achieves a high 99.8% EHL conversion and a high yield of 169.5 mg per g EHL to cycloalkanes, which breaks the limit of C–O bonds.[8] In Fig. 4b, the total ion chromatogram (TIC) of the EHL conversion product of $Ni_9Fe_1/NiAlO_z$ catalyst shows the peaks of cyclohexane, methyl, ethyl, propyl, and butyl cyclohexane, with trimethylbenzene as the internal standard. The product in the absence of a catalyst contains 4-propylguaiacol, isoeugenol, dihydroconiferyl alcohol, coniferyl alcohol and 5-(3-hydroxypropyl)-2,3-dimethoxyphenol. The EHL product mixture was characterized by 2D-HSQC NMR spectroscopy. In Fig. 4c, the HSQC result shows that the solvent-treated lignin is mainly composed of β-O-4 bonds, with small amounts of β–β and β-5 bonds. The signals at δ_C/δ_H 75.1/4.92 ppm and 88.3/4.23 ppm are from the β-O-4 bonds.[15] C_α and C_β, at δ_C/δ_H 70.2/3.43 ppm, δ_C/δ_H 79.6/3.80 ppm and δ_C/δ_H 61.2/3.44 ppm, represented the

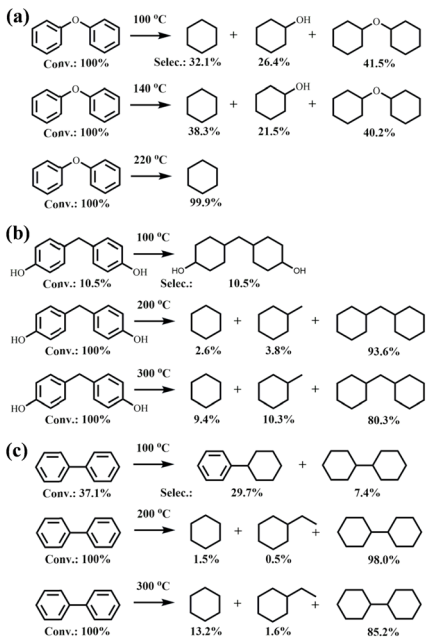

Fig. 3 Catalytic cleavage results of (a) 4-O-5, (b) α-4, and (c) 5–5 bonds of various dimers over the $Ni_9Fe_1/NiAlO_z$ catalyst. Reaction conditions: 500 mg catalyst, 500 mg dimer, 0.8 MPa H_2, 3 h, and 70 mL *n*-dodecane.

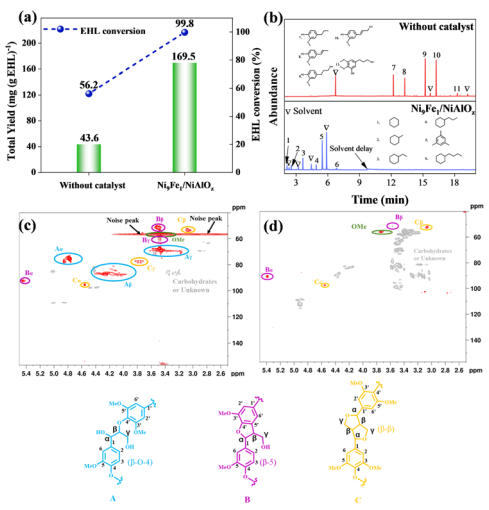

Fig. 4 (a) Monomers yield and (b) the total ion chromatogram (TIC) and structures of the detected products obtained from the EHL conversion without or with $Ni_9Fe_1/NiAlO_z$ catalyst. HSQC characterizations of (c) lignin oil from EHL without a catalyst and (d) the lignin oil product from the $Ni_9Fe_1/NiAlO_z$-catalyzed depolymerization reaction. A represents β-aryl ether, while B denotes phenylcoumaran substructures formed by the β-5 bond, and C denotes resinol substructures formed by the β–β bond. Reaction conditions: 500 mg catalyst, 500 mg EHL, 300 °C, 3 MPa H_2, 6 h, and 70 mL *n*-dodecane.

A_γ-OH, C_γ-OH and B_γ-OH, and the OMe (aromatic-OMe) signal located at δ_C/δ_H 58.4/3.4 ppm.[15] After depolymerisation of $Ni_9Fe_1/NiAlO_z$ at 300 °C for 6 h, a significant change in the structure is observed in Fig. 4d. The signal of γ-OH in A_γ, B_γ and C_γ is not found; the signals in the region of OMe decreases, and β-O-4 even disappears. However, some residues of C–C bonds, including C_α and C_β in the C structure and B_α and B_β in the B structure, are detected. The $Ni_9Fe_1/NiAlO_z$ can effectively participate in breaking C–O and OMe bonds (aromatic ring hydrogenation) and removing γ-OH, achieving the complete HDO. However, there are still deficiencies in dealing with C–C bond breakage.

3.2 Results of *in situ* characterization

In situ EPR curves during the PPE hydrogenation reaction are shown in Fig. 5a. The catalyst before PPE adsorption shows a strong characteristic signal at $g = 2.003$, which has been assigned as the oxygen vacancies (OVs).[20] The EPR curve gives a straight line for the mixture of PPE and $Ni_9Fe_1/NiAlO_z$ at 25 °C, without any signal in the range. In the temperature range of 25 to 100 °C, this signal characterizing the amount of OVs increases, indicating the surface reaction and desorption of the oxygen species. The measurement was prolonged at 100 °C, and an enhancement of the OVs signal with time online is observed, implying the intensive elimination of the oxygen species simultaneously with the formation/desorption of cyclohexanol and ethylcyclohexane. The maximum value of the OV signal is achieved at 3 h; however, this value is lower than that of the pristine catalyst. As shown in Fig. 5b, the post-reaction catalyst in oxygenated solvent has a lower OV content than that in dodecane solvent, and the post-reaction catalyst in dodecane solvent has the EPR signal closest to the EPR signal of the fresh catalyst.

After adsorbing PPE on the surface of $Ni_9Fe_1/NiAlO_z$, FT-IR spectra were collected at different temperatures and time intervals under H_2 flow. In Fig. 5c, the peaks at 1037.5, 1492.8, and 1600.6 cm^{-1} are attributed to the symmetrical stretching vibration of the C–O–C ether bond, bending, and stretching vibration of the benzene ring, respectively.[21,22] The peaks at 1243.8, 1725.9, and 3410.5 cm^{-1} correspond to the stretching vibration of –OH in the phenolic hydroxyl, C=O bond in the aldehyde, and –OH in alcohol hydroxyl groups, respectively.[22,23] With an increase in temperature from 25 to 100 °C, the intensity of the phenol peak gradually increases, whereas the peak of the C–O–C ether bond weakens. Subsequently, with the increase in time from 1 to 3 h at 100 °C, the peak corresponding to the alcohol hydroxyl group appears, and the peaks of the benzene ring, C–O–C ether bond, and phenolic hydroxyl group gradually weaken. The C–O–C ether bond of PPE is hydrogenated and broken, generating phenol and ethylbenzene. Meanwhile, the peaks due to the C=O bond and alcohol hydroxyl group appear at 1 h, and the C=O bond peak disappears at 3 h, whereas the peak due to the alcohol hydroxyl group remains. Phenol undergoes benzene ring hydrogenation, generating ketone intermediates and the formation of cyclohexanol. The gradual decrease in the peak intensity corresponding to the benzene ring demonstrates the hydrogenation of ethylbenzene. Additionally, the peaks corresponding to aliphatic hydrocarbons are not detected because of their weak adsorption.

3.3 Catalyst characterization

3.3.1 Fine structures of the catalysts. As illustrated in Fig. 6a, the peaks in the XRD patterns are attributed to the NiFe-LDH (PDF#38-0715) phase for the Ni_9Fe_y-LDH catalyst precursors. Similarly, for the NiAl-LDH sample, the diffraction peaks belong to the NiAl-LDH phase (PDF#15-0087). No diffraction peak was detected in the $FeAl(OH)_x$ sample. After calcination in air at 500 °C, the LDH phase was decomposed; the OH^-, NO^{3-}, and H_2O groups were eliminated; and the LDH structure was transformed into a mixed oxide phase. In Fig. 6b, only NiO (2θ = 37.3°, 43.3°, and 62.9°, PDF#47-1049) diffraction peaks are visible in $NiAlO_z$ catalyst. Only small diffraction peaks are

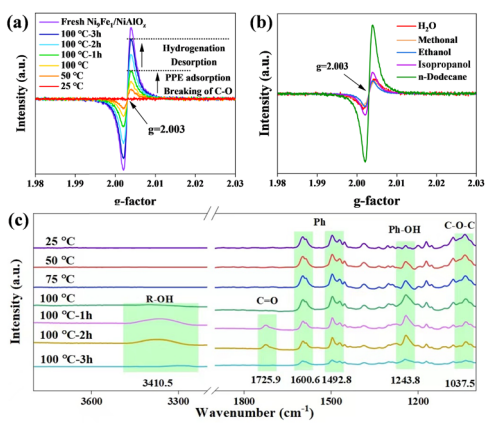

Fig. 5 (a) *In situ* EPR results for PPE HDO over the $Ni_9Fe_1/NiAlO_z$ by the flowing H_2 with increasing reaction temperature. (b) EPR results of $Ni_9Fe_1/NiAlO_z$ after reaction with different solvents. (c) *In situ* FT-IR spectra of contents in the PPE HDO over the $Ni_9Fe_1/NiAlO_z$ by the flowing H_2 with increasing reaction temperature.

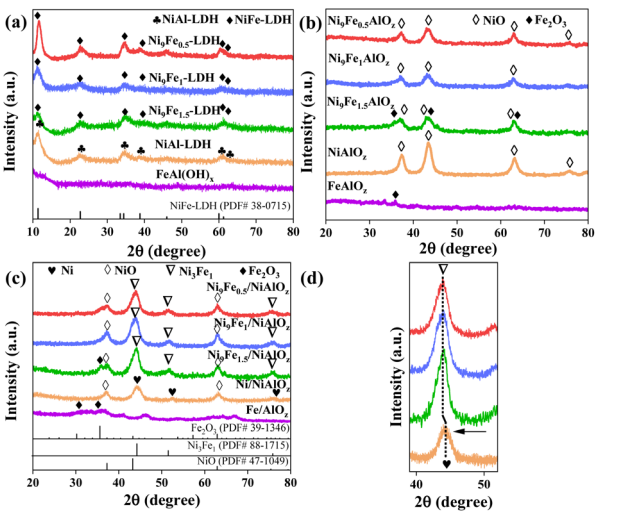

Fig. 6 XRD patterns of (a) Ni_xFe_y-LDH, (b) $Ni_xFe_yAlO_z$ and (c) $Ni_xFe_y/NiAlO_z$. (d) Details of 40–50° in $Ni_xFe_y/NiAlO_z$.

identifiable, belonging to the phase Fe_2O_3 in the pattern of the $FeAlO_x$ catalyst. The XRD patterns of the samples after reduction ($Ni_xFe_y/NiAlO_z$) are shown in Fig. 6c. The identifiable peaks are attributed to Ni ($2\theta = 44.5°$, 76.3°, PDF#04-0850) and NiO for the $Ni/NiAlO_z$ samples. The diffraction peaks of Fe_2O_3 (PDF#39-1346) appear in the Fe/AlO_z sample. The peaks of both Ni_3Fe_1 and NiO phases are present in all the $Ni_9Fe_y/NiAlO_z$ samples. The peaks at $2\theta = 44.2°$, 51.5°, and 75.8° belong to the Ni_3Fe_1 phase (PDF#88-1715) and at $2\theta = 37.3°$ and 62.9° belong to the NiO phase. The diffraction peaks attributed to Fe_2O_3 are significantly observed in $Ni_9Fe_{1.5}/NiAlO_z$ but not in $Ni_9Fe_{0.1}/NiAlO_z$ and $Ni_9Fe_{1.5}/NiAlO_z$. There is no peak of Al_2O_3 observable in all catalysts. In Fig. 6d, compared to the $Ni/NiAlO_z$, the diffraction peaks of Ni at $2\theta = 44.5°$ in $Ni_9Fe_y/NiAlO_z$ samples shift to a lower degree, indicating the formation of NiFe alloy.[24]

The XANES spectra at the Ni and Fe K-edges, depicted in Fig. 7a and b, reveal distinctive near-edge patterns situated between the reference curves of Ni foil, NiO, and Fe foil, Fe_2O_3. These unique features are different from those of Ni foil and Fe foil and coupled with the emergence of the absorption shoulder edges similar to oxides, suggesting a near-edge structure similar to those of oxides (Fig. S2†). In Fig. 7a, the white line intensities gradually decline in the order of $Ni_9Fe_1/NiAlO_z$ and $Ni/NiAlO_z$, reflecting the electron-rich characteristics exhibited by the Ni species in $Ni_9Fe_1/NiAlO_z$. Fig. 7b shows a lower white line intensity for the Fe K-edge in $Ni_9Fe_1/NiAlO_z$ compared to Fe/AlO_z, which suggests that the Fe species in $Ni_9Fe_1/NiAlO_z$ exhibits a more electron-deficient character.[25,26] Electron redistribution occurs between Ni and Fe and results in electron-rich Ni species in $Ni_9Fe_1/NiAlO_z$.

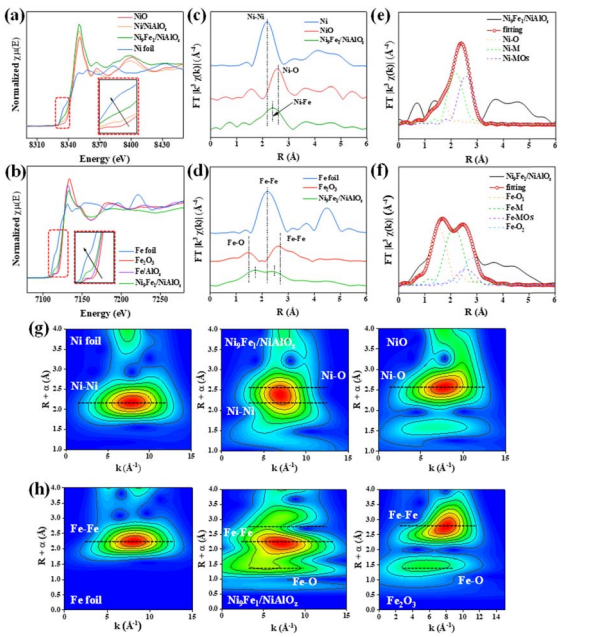

Fig. 7 (a) Ni and (b) Fe K-edge XANES spectra of $Ni_9Fe_1/NiAlO_z$ and reference samples. (c) Ni and (d) Fe K-edge FT-EXAFS spectra of $Ni_9Fe_1/NiAlO_z$ and reference samples. EXAFS (e) Ni and (f) Fe R-space fitting curves of $Ni_9Fe_1/NiAlO_z$. The plots are not corrected for the phase shift. WT-EXAFS of (g) Ni foil, $Ni_9Fe_1/NiAlO_z$, and NiO; and (h) Fe foil, $Ni_9Fe_1/NiAlO_z$, and Fe_2O_3.

Fig. 6c–f demonstrates the R-space data of the k^2-weighted Ni and Fe K-edge Fourier transform EXAFS (FT-EXAFS) spectra of the corresponding reference samples, $Ni_9Fe_1/NiAlO_z$ and its fitting data. A single prominent coordination scattering peak at 2.4 Å, interposed between the Ni foil (2.1 Å) and NiO (2.6 Å) peak positions, is observed in Fig. 7c for $Ni_9Fe_1/NiAlO_z$. In addition, the XANES threshold for Ni in the $Ni_9Fe_1/NiAlO_z$ shifted slightly to lower energies compared to the NiO, suggesting the formation of a Ni–M bond with a distance of 2.4 Å. Fe–Fe (2.5 Å) is present in Fe foil, while Fe–O (1.4 Å) and Fe–Fe (2.7 Å) in Fe_2O_3. In Fig. 7d, there are Fe–Fe and Fe–O bonds, but the Fe coordination environment changes and the corresponding bond lengths change to 1.7 Å for Fe–O and 2.4 Å for Fe–M, forming strong evidence for the existence of Ni–Fe bonds as the NiFe alloy phase. The absence of Ni–Ni and Fe–Fe peaks and the fact that the Ni–M and Fe–M bonds in $Ni_9Fe_1/NiAlO_z$ are displaced indicate the presence of a NiFe alloy phase and an M–O–M oxide structure. In Fig. 7d, the peak position of Fe–O in Fe_2O_3 is lower than that of $Ni_9Fe_1/NiAlO_z$, and the Fe–Fe bond is not found. The changes in the Fe–O and Fe–Fe bonds are clear evidence of the formation of the NiFe alloy.

In Table S2,† the coordination numbers of Ni (Ni–M, Ni–O) in $Ni_9Fe_1/NiAlO_z$ are consistent with Ni and NiO, and this means that Ni species form the main part of the catalyst. The Fe–M coordination numbers of 6 and 5.8 in Table S3† indicate the absence of a full metal alloy, and a considerable number of Fe–O bonds appear, making it easier to generate multiple types of OVs. Fitting calculations to the R-space data of $Ni_9Fe_1/NiAlO_z$ catalyst are shown in Fig. 7e and f. In Fig. 6e, bonds located at 1.6 Å for Ni–O, 2.2 Å for Ni–M (distinguished from 2.1 Å for the Ni–Ni bond in the Ni foil), and 2.6 Å for Ni–MOs appear. In Fig. 7f, 1.5 Å of Fe–O_1, 2.2 of Fe–M (distinguished from 2.17 Å of Fe–Fe bond in Fe foil), 2.6 Å of Fe–MO and 2.8 Å of Fe–O_2 appear. The bond lengths of Ni–Fe in the fitted data for Ni and Fe–Ni in the fitted data for Fe are consistent with each other, as well as with Ni–MOs and Fe–MOs. The data indicate that Ni–Fe interacts closely with each other, forming the NiFe alloy and rich interface. The wavelet transform, with its pronounced differentiation in R spaces, serves as a complementary tool to FT-EXAFS for the microstructure determination of the catalyst metal phases. The K-edge WT-EXAFS for Ni and Fe are depicted in Fig. 7g and h, respectively. The coordination profiles of Ni and Fe change, and the regions of the corresponding bonds change. In this case, the Ni–M region in the catalyst is in the middle of Ni foil and NiO, and the change in the Fe coordination situation is more obvious, appearing in the Fe–O region and region change in Fe–M compared to Fe foil and Fe_2O_3. Moreover, quantitative FT-EXAFS fits were carried out to reveal structural parameters, as demonstrated in Tables S2 and S3.† The results indicate a high degree of fit, exhibiting an R factor of less than 0.009 and an internal potential correction (ΔE_0) of less than ±10 eV. The catalysts show larger Ni–M bond lengths (2.6 Å/3.0 Å) than those of Ni foils (2.5 Å), with Fe showing a similar trend to that of Ni, and this directly proves the formation of the NiFe alloy phase.

3.3.2 Ability to activate hydrogen. The H_2-TPR profiles are plotted in Fig. 8a. For the $Ni/NiAlO_z$ sample, the broad and

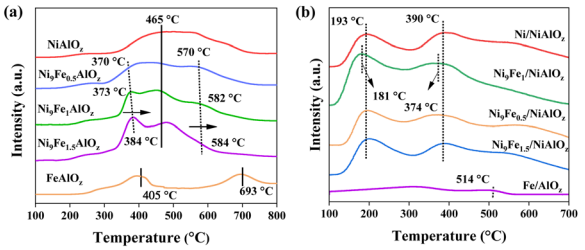

Fig. 8 H_2-TPR (a) and H_2-TPD (b) results of the catalysts.

diffused H_2 consumption peak (400–800 °C) corresponds to the reduction of NiO to different particle sizes.[16] H_2 consumption peaks at 405 °C (for Fe_2O_3 to Fe_3O_4) and 693 °C (for FeO to α-Fe) are observed for the Fe/AlO_z sample. For the Ni_9Fe_1/$NiAlO_z$, three H_2 consumption peaks are observed at approximately, 373, 465, and 582 °C, as illustrated in Fig. 8a. The first peak at approximately 370 °C may be associated with the reduction of small Fe_2O_3 particles on the surface.[27,28] The second peak at 465 °C represents the simultaneous reduction of Ni and Fe oxides and the subsequent formation of the NiFe alloy.[29] Because the effective dissociation of H_2 on Ni_3Fe_1 accelerated the FeO_x species reduction, Ni_9Fe_1/$NiAlO_z$ exhibits a peak at a considerably lower temperature of approximately 582 °C, compared to the peak at 693 °C for Fe/AlO_z.[30,31] In Fig. 8a, the peaks near 370 and 570 are observed to undergo gradual displacement towards higher temperatures from $Ni_9Fe_{0.5}$/$NiAlO_z$ to $Ni_9Fe_{1.5}$/$NiAlO_z$, thereby demonstrating that the reduction of the iron oxide is more challenging.

In Fig. 8b, the H_2-TPD profiles of the Ni/$NiAlO_z$ sample show two peaks at 193 and 390 °C, while the Ni_9Fe_1/$NiAlO_z$ catalyst exhibits two peaks at lower temperatures than those of the Ni/$NiAlO_z$ sample, at 181 and 374 °C. The presence of peaks at 181 and 374 °C in the TPD curve of the Ni_9Fe_1/$NiAlO_z$ sample may represent the desorption of chemisorbed hydrogen from the Ni–H species and from H* on the Ni surface, respectively.[32] The Fe/AlO_z sample demonstrates only one weak desorption peak at 514 °C. In Fig. 8b, $Ni_9Fe_{0.5}$/$NiAlO_z$ and $Ni_9Fe_{1.5}$/$NiAlO_z$ samples also give two peaks at 200 and 388 °C in their H_2-TPD curves, but both the two peaks on the two curves appear later than those of Ni_9Fe_1/$NiAlO_z$. Table 2 lists the overall H_2 uptakes of the samples in H_2-TPD. Ni/$NiAlO_z$ takes 0.41 mmol g^{-1} higher than that of Fe/AlO_z sample, 0.34 mmol g^{-1}. Higher H_2 uptake is detected for the $Ni_9Fe_{0.5}$/$NiAlO_z$, 0.44, and $Ni_9Fe_{1.5}$/$NiAlO_z$, 0.42 mmol g^{-1}, samples, suggesting that the optimized Fe amount favors H_2 adsorption.[33] Ni_9Fe_1/$NiAlO_z$ has the highest H_2 absorption rate of 0.51 mmol g^{-1}, which provides the possibility for low temperature and high efficiency HDO reaction.

Table 2 Composition, BET and H_2-TPD results of catalysts

Catalysts	Ni/Fe ratio[a]	Ni/Fe ratio[b]	S_{BET} (m^2 g^{-1})	H_2 uptake ($mmol_{H_2}$ g^{-1})
Ni/$NiAlO_z$	—	—	78.6	0.41
$Ni_9Fe_{0.5}$/$NiAlO_z$	17.6	—	181.5	0.44
Ni_9Fe_1/$NiAlO_z$	8.9	9.8	325.7	0.51
$Ni_9Fe_{1.5}$/$NiAlO_z$	6.3	—	156.6	0.42
Fe/AlO_z	—	—	28.9	0.34

[a] The results are tested by ICP. [b] These results are obtained from SEM-EDS mapping.

The intensity of the hydrogen spillover was examined with the color change in the samples, as depicted in Fig. S3.† Initially, the mixture of catalyst samples and WO_3 showed an identical bright yellow color. After 30 s of exposure to the hydrogen atmosphere, all the three samples changed their color. Fe/AlO_z mixture still showed yellow, but the Ni/$NiAlO_z$ mixture had already turned grayish green, and the Ni_9Fe_1/$NiAlO_z$ mixture became dark blue. After 180 s, the Ni_9Fe_1/$NiAlO_z$ mixture was black, and the Ni/$NiAlO_z$ mixture turned into a bluish-gray, while Fe/AlO_z had a sallow-like color. The rapidness of the color change indicates the strength of the hydrogen spillover phenomenon. Ni_9Fe_1/$NiAlO_z$ is the strongest, while Fe/AlO_z is the weakest with Ni/$NiAlO_z$ in the middle.

3.3.3 Microscopic and surface electronic structures. Fig. 9a–c gives the SEM micrographs. The Ni_9Fe_1/$NiAlO_z$ sample has a lamellar structure with an average thickness of around 57 nm. Ni/$NiAlO_z$ shows a fragmented sheet structure, and Fe/AlO_z exhibits large clusters of particles and is not laminated. The representative nanoparticle scans in Fig. 9d display lattice stripes at distances of 0.206 and 0.238 nm, which are consistent with Ni_3Fe_1 (111) and NiO (003) lattice planes, respectively (details in Fig. S4†). The STEM-EDS linear scanning and mapping results in Fig. 9e and f demonstrate the specific elemental distribution state of Ni, Fe, and Al, revealing that Fe concentrates in the center of the particles, while Ni and Al disperse uniformly throughout, forming the core–shell structure.

The Brunauer–Emmett–Teller (BET) specific surface area, catalyst composition and texture data are listed in Table 2. Ni_9Fe_1/$NiAlO_z$ sample has the largest specific surface area of 325.7 m^2 g^{-1}. The contents of Ni and Fe in Ni_9Fe_1/$NiAlO_z$

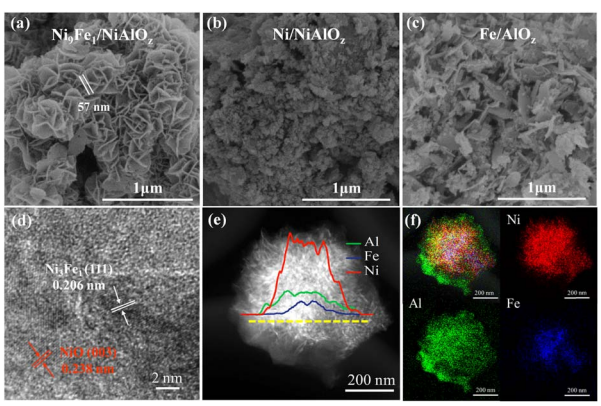

Fig. 9 SEM images of (a) Ni_9Fe_1/$NiAlO_z$, (b) Ni/$NiAlO_z$ and (c) Fe/AlO_z. (d) HRTEM image and (e) TEM image and line scanning of Ni_9Fe_1/$NiAlO_z$. (f) Elemental mappings of Ni_9Fe_1/$NiAlO_z$.

catalyst measured with the ICP technique are 47.83% and 10.89%, respectively, which are consistent with the prescription, indicating no loss of metals during the preparation procedure. Table 2 shows the SEM-EDS analysis of $Ni_9Fe_1/NiAlO_z$ catalyst surface composition, differing from the ICP analysis results of the bulk composition. The surface of the sample is Ni-enriched with a Ni/Fe ratio exceeding 9/1. Corroborating EDS mapping in Fig. 9f and ICP bulk analysis results, in Table 2, Fe is located in the interior of the particles.

For the Ni $2p_{3/2}$ XPS spectrum of the $Ni_9Fe_y/NiAlO_z$ catalyst (Fig. 10a), the peaks at 852.6, 855.5, and 862.1 eV belong to Ni^0, Ni^{2+}, and a satellite peak, respectively.[34] The Fe $2p_{3/2}$ XPS pattern (Fig. 10b) shows three peaks at 705.2, 711.3, and 714.3 eV, corresponding to Fe^0, Fe^{2+}, and Fe^{3+}, respectively.[35] The binding energy of Ni^0 in $Ni/NiAlO_z$ is 0.3 eV higher than that in $Ni_9Fe_1/NiAlO_z$, and the binding energy of Fe $2p_{3/2}$ in $Ni_9Fe_1/NiAlO_z$ catalyst exhibits a positive shift (0.4 eV) to that of the Fe/AlO_z. The XPS results of Ni 2p and Fe 2p demonstrate that electrons are transferred from Fe to Ni.

The high-resolution O 1s spectra of the $Ni_xFe_y/NiAlO_z$ samples are illustrated in Fig. 10c. The peaks at 530.2 eV ($O_{(I)}$), 531.8 eV ($O_{(II)}$) and 532.8 eV ($O_{(III)}$) are attributed to lattice oxygen, OVs, and chemisorbed oxygen, respectively.[36,37] The ratios of OVs in different samples are presented in Fig. 10c. The OV ratios of $Ni_9Fe_y/NiAlO_z$ samples are considerably higher than those of $Ni/NiAlO_z$ (0.33) and Fe/AlO_z (0.31). The content of OVs increases and then decreases with the increase in doped Fe content, where it is 0.37 for $Ni_9Fe_{0.5}/NiAlO_z$ and 0.35 for $Ni_9Fe_{1.5}/NiAlO_z$ and takes the maximum with the $Ni_9Fe_1/NiAlO_z$ (0.41). The OV concentrations are validated using the EPR technique, and the results are plotted in Fig. 10d, exhibiting that the signal strengths of the OVs ($g = 2.003$) show the same sequence as shown by the XPS technique,[20] which confirms that the incorporation of a suitable amount of Fe leads to more OVs.

For the $Ni_xFe_y/NiAlO_z$ samples, FT-IR analysis was performed with CO adsorption (see Fig. 10e). The Fe/AlO_z sample did not adsorb CO. Typically, CO adsorption on Ni sites can be categorized into two distinct types: bridge type, at frequencies below 1980 cm^{-1}, and linear type, in the frequency range above 2050 cm^{-1}.[38] A linear adsorption peak, approximately 2058 cm^{-1}, and a bridge peak, 1954 cm^{-1}, of $Ni/NiAlO_z$ are observed in Fig. 10e. The linear, now at 2047 cm^{-1}, and bridge, 1943 cm^{-1}, adsorption peaks of $Ni_9Fe_y/NiAlO_z$ are redshifted compared to those of the $Ni/NiAlO_z$ sample, also indicating electron transfer from Fe to Ni atom.

3.3.4 Characterization of the catalyst used. Fig. 11a shows the TG results under airflow of the fresh and the used one (P–$Ni_9Fe_1/NiAlO_z$) in the PPE hydrogenation reaction. The volatile component is lost up to a temperature of 142.7 °C, and the oxidation of the Ni and Fe components occurs up to 364.5 °C. The weight of the fresh catalyst increased by 6.2 wt%, while that of the P–$Ni_9Fe_1/NiAlO_z$ sample increased by only 3.1 wt%, indicating that the fresh catalyst has a higher content of low-valent Ni or Fe species than that of the P–$Ni_9Fe_1/NiAlO_z$.[39] Fig. 11b illustrates no significant differences in the Raman spectra between the fresh and P–$Ni_9Fe_1/NiAlO_z$ catalysts, and two peaks belonging to the D (indeterminate carbon) and G (graphitic carbon) bands at 1383.7 and 1601.6 cm^{-1} were not observed, confirming that the P–$Ni_9Fe_1/NiAlO_z$ catalyst is free of coke.[40] In Fig. 11c, the EPR results show a negligible change in the catalyst OV concentrations between the fresh and P–$Ni_9Fe_1/NiAlO_z$ catalysts. In Fig. 11d and e, the SEM image and the EDS mapping of the P–$Ni_9Fe_1/NiAlO_z$ catalyst show clear laminar structures with elemental distributions consistent with those of the fresh catalyst (Fig. 8f). Fig. 11f depicts no significant differences in the XRD patterns between the fresh and P–$Ni_9Fe_1/NiAlO_z$ samples. The crystal structure of the $Ni_9Fe_1/NiAlO_z$ catalyst is sufficiently stable in the PPE cyclic reactions.

4 Discussion

A key finding of our study is the ability to fully depolymerize PPE, a common β-O-4 bonds that represent compounds, into

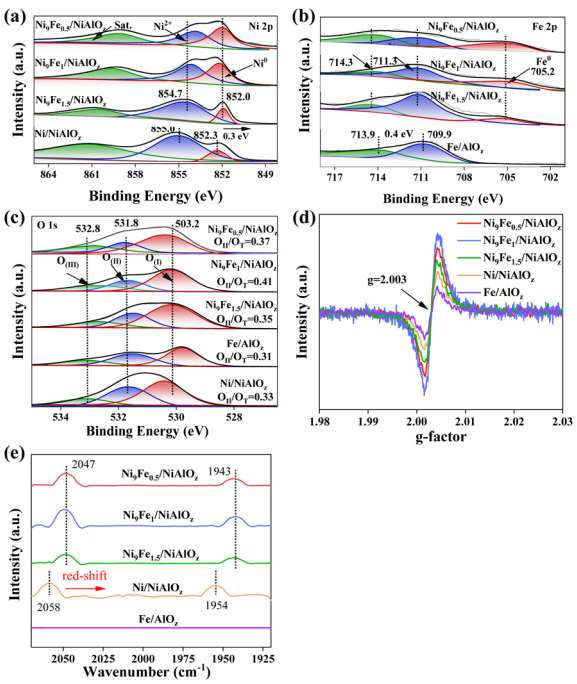

Fig. 10 Deconvoluted XPS spectra of the (a) Ni 2p, (b) Fe 2p and (c) O 1s from the $Ni_xFe_y/NiAlO_z$ samples. (d) EPR patterns; (e) CO-DRIFT curves of $Ni_xFe_y/NiAlO_z$.

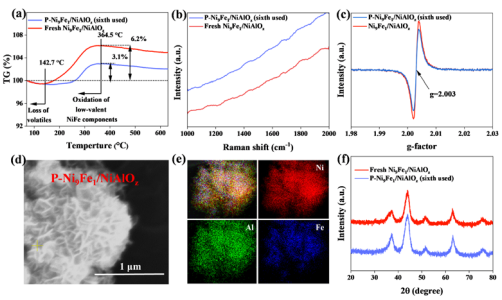

Fig. 11 (a) TG curves of the fresh and P–$Ni_9Fe_1/NiAlO_z$ catalyst. (d) SEM and (e) elemental mapping of P–$Ni_9Fe_1/NiAlO_z$. (b) EPR results, (c) Raman results, and (f) XRD patterns of the fresh and P–$Ni_9Fe_1/NiAlO_z$.

alkanes under exceptionally mild conditions (100 °C, 0.8 MPa H_2, and 3 h). Although previous efforts have achieved partial lignin depolymerization or the conversion of model linkages at higher temperatures (150–300 °C), none have shown complete decomposition to single compounds below 150 °C (Table S4†). Notably, our Fe–Ni catalyst surpasses the traditionally used monometallic systems. The synergistic hydrogen activation inferred from numerous characterized structures demonstrates that the catalytic configuration of the alloy-coupled oxygen vacancies greatly facilitates hydrogenation and deoxygenation reactions. The activity exhibited by our simple, scalable catalyst system compares favourably even with more advanced nanomaterials. In summary, this study demonstrates the most active lignin model compound depolymerization reported to date, highlighting the potential of multi-locus cooperativity between transition metals to advance biomass upgrading.

4.1 Catalytic performance

Analysis of PPE deoxygenation product distributions at 100 °C, 140 °C, and 300 °C revealed that 100 °C selectively cleaves C–O bonds and saturates aromatic rings, whereas higher temperatures completely remove oxygen. Mono-Fe and mono-Ni catalysts exhibited substantially lower activity than the bifunctional $Ni_9Fe_1/NiAlO_z$ catalyst containing a Ni_3Fe_1 alloy phase, confirming that the alloy enables cooperative C–O activation *via* intimate Ni–Fe interfaces (Table 1).[33] The predominant products at 80 °C (Fig. 2a) and 0.4 MPa H_2 (Fig. 2b) cyclohexanol and ethylbenzene, respectively, suggest that the active sites selectively cleave the C–O bond to phenol while saturating the aromatic ring to cyclohexanol without hydrogenating the ethylbenzene ring. The combination of the reaction results with different hydrogen pressures and *in situ* FT-IR/EPR shows that temperature is crucial for the reaction, and both mobile and fixed hydrogen are efficiently involved in the reaction. Moreover, the reaction progress could be tuned by time to selectively optimize the yields of ethylbenzene, cyclohexanol, or cyclohexane–cyclohexanol mixtures (Fig. 2c). Near-complete conversion within 2 to 3 h (Fig. 2d) validated the high activity attributable to abundant active sites. Ethylbenzene hydrogenation at elevated temperatures benefited from sufficient energy and hydrogen supply. As the reaction intensity increases (higher temperature, higher H_2 pressure and longer time), ethylcyclohexane/cyclohexane and cyclohexanol become the major products, indicating that the hydrogenation reaction occurs sequentially, rather than simultaneously, at different spatially active sites on the catalyst surface.

The differential reactivity of dimers provides insight into the catalyst's distinct handling of C–O *versus* C–C bonds. At 100 °C, Fig. 3a shows that aromatic hydrogenation predominates for diphenyl ether over sluggish C–O cleavage, limited by ether oxygen ligation. In contrast, Fig. 3b demonstrates efficient dehydroxylation and ring hydrogenation for the 4,4′-dihydroxydiphenylmethane, attributed to phenolic hydroxyl group participation. Fig. 3c shows that although biphenyl did not undergo bond cleavage, aromatic hydrogenation alone enabled a conversion of 37.1%. Biphenyl has a higher reactivity at low temperatures compared to 4-phenylphenol (Fig. S1†), and this higher reactivity can be attributed to the lack of oxygen, which reduces competitive adsorption and thus promotes hydrogenation. Temperature effects observed for PPE transformations similarly impacted various dimers. Sufficient energy facilitated the complete cleavage of the C–O bond and fully hydrogenated products in diphenyl ether, alongside the cleavage of the C–C bond yielding alkylcycloalkanes. However, most C–C dimers converted to fully saturated bicyclic alkanes without bond cleavage.

The EHL reaction produced a monomer of 169.5 mg per g EHL, with the remaining oligomer undetectable by GC-MS. However, the monomer yield exceeded the theoretical yield obtained from all C–O bond breaks in EHL, with excess coming from C–C bond break products. In the NMR results (Fig. 4c and d), the disappearance of the β-O-4 bond signal region and the attenuation of the –OMe signal region proved that the catalyst could achieve effective HDO, and the reduction of the C–C bond signal region provided evidence for monomer yields beyond the theoretical yields.[8,15]

4.2 Structure of the catalyst

The $Ni_9Fe_1/NiAlO_z$ catalyst exhibits superior hydrogenation and deoxygenation performance towards the conversion of PPE and EHL. This stems from the synergistic interplay between a high concentration of OVs and abundant Ni–Fe active sites. At the atomic scale, the mixed oxide phase features a unique two-dimensional layered (2DL) architecture in $Ni_9Fe_1/NiAlO_z$, which is rich in interfacial OVs around the NiFe alloy clusters. This increases the contact probability of reactants by increasing the step, corner and edge densities. The enlarged surface area and defects give the catalyst a higher H_2 adsorption capacity, which is a key to activating and supplying hydrogen. In addition, the core–shell structure, in which the Ni site is fully exposed and the Fe with weak hydrogenation activity is coated, is combined with the 2DL structure, which strengthens the H adsorption ability.[10]

The specific adsorption of substrates and the activation of H are then related to the refined sites in the catalyst. According to the results of XAFS and XRD, $Ni_9Fe_1/NiAlO_z$ has Ni_3Fe_1 alloy phase and the appropriate distance of Ni–Fe bond, which is conducive to the stability of the catalyst. Nearby, enriched NiFe sites generated from Fe–doping induce the formation of dispersed ordered Ni_3Fe_1 alloy clusters, and these active phases readily dissociate H_2 and spill over H, OH and oxygen species. In addition, the coordination of Ni and Fe contains Ni–O and Fe–O bonds, suggesting that a large amount of M–O is contained outside the coordinating atoms of Ni_3Fe_1, which directly leads to the formation of abundant interfacial OVs and promotes H transport and activation.[33] The results of XPS and CO-DRIFTS also proved that electron transfer from Fe tunes the electronic states of Ni to further boost its hydrogenation functionality. The results of the H_2-TPR, H_2-TPD, and WO_3 discoloration experiments particularly demonstrate this, with high-velocity hydrogen spillover occurring in the catalysts in conjunction with a high content of OVs, to the extent that it serves as high

hydrotreating activity in the later hydrogenation reactions of EHL and PPE.[32,41] $Ni_9Fe_1/NiAlO_z$ catalyst tends to saturate the carbon–oxygen bond more than the aromatic ring at first, thus simplifying the product distribution. Cooperative interactions between OVs, Ni–Fe alloy and adjusted surface chemistry collectively endowed the $Ni_9Fe_1/NiAlO_z$ with unrivalled activity for the challenging transformation of EHL and lignin derivatives.

4.3 Relationship of structural activity

Table 1 shows catalysts $Ni_9Fe_1/NiAlO_z$ and Fe/AlO_z differing in activity for PPE conversion, with $Ni_9Fe_1/NiAlO_z$ (Ni_3Fe_1) significantly outperforming Fe/AlO_z ($FeAlO_z$). Catalysts $Ni/NiAlO_z$ and $Ni_9Fe_1/NiAlO_z$ contain different nickel species, and $Ni_9Fe_1/NiAlO_z$ (Ni_3Fe_1) catalyzes PPE at a much higher rate than $Ni/NiAlO_z$ catalyst (single Ni). Nickel sites facilitate C–O bond breaking. Ni_3Fe_1 contains both electron-rich Ni and electron-deficient Fe, and the ability to activate H is much higher than that of single Ni. Moreover, the $Ni/NiAlO_z$ catalyst has few OVs, limiting C–O bond adsorption and yielding irregular products.[10]

$Ni_9Fe_1/NiAlO_z$ catalyst abundantly contains OVs around Ni_3Fe_1 that preferentially coordinate the C–O bond, directing its reaction through a streamlined pathway. The results in Fig. 5a and b illustrate the importance of OVs as important adsorption and hydrogenation sites. The former is shown by the *in situ* EPR results that the disappearance of OVs due to the complete adsorption of PPE at the beginning of the reaction, but the huge increase in the number of OVs at 2 h and 3 h is due to the desorption of cyclohexanol in the product. The latter is evident from the experimental data of PPE conversion in different solvents (Table S1†), which shows that the occupation of OVs greatly slows down the hydrogenation bond-breaking reaction. The core–shell structure of the $Ni_9Fe_1/NiAlO_z$ catalyst encapsulates the hydrogenation-inert Fe cores, exposing oxygen-vacancy-rich MO shell sites that promote surface H_2 adsorption. As evidenced by temperature-programmed reduction and X-ray absorption fine structure spectroscopy, the robust interface between Ni_3Fe_1 cores and shells facilitates the stabilization of active catalytic sites with excellent reproducibility.[42] The OV-rich shells are hypothesized to spillover hydrogen to Ni_3Fe_1 catalytic sites, generating highly reactive hydrogen species to enable regioselective C–O cleavage and aromatic ring hydrogenation.[43,44] Notably, the synergistic cooperation between Ni_3Fe_1 and interfacial OVs in $Ni_9Fe_1/NiAlO_z$ catalyst is vital for efficient PPE conversion, outperforming single-component catalysts.

The specific reaction pathway for PPE in Scheme 2 is shown by summarizing the data in Subsection 3.1 (Fig. 1 and 2) and *in situ* FT-IR. The bond of C–O–C breakage followed this path: (1) C–O bond cleavage preferentially produced alkylphenols and arenes; (2) alkylphenols underwent ring saturation; (3) arenes underwent hydrogenative ring saturation; and (4) if the energy is sufficient, cyclohexanol dehydroxylates to form cyclohexane. (2-Cyclohexyloxy)benzene and (2-(cyclohexyloxy)ethyl)benzene were not detected throughout the reaction of PPE, indicating that the C–O bond in PPE is firmly adsorbed onto the interfacial oxygen vacancies composed of Fe atoms. This adsorption

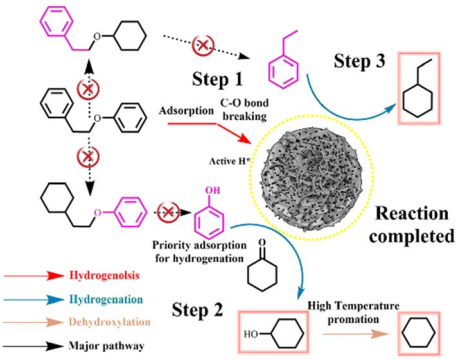

Scheme 2 Proposed reaction pathway for the PPE conversion over the $Ni_9Fe_1/NiAlO_z$ catalyst.

weakens the C–O bond energy, leading to the initial bond cleavage occurring before the hydrogenation of the aromatic ring. Even though the Ni sites have a good adsorption capacity for aromatic rings, the same is true for the preferential hydrogenation of phenol over ethylbenzene, and the involvement of the sites constituted by Fe is the fundamental reason the catalyst can produce specificity. Overall, judicious engineering of the bimetallic core–shell interface and attendant defects optimizes catalytic architectures for challenging biomass upgrading transformations. Further studies will provide deeper insights into reaction mechanisms and guide the design of specialized catalyst systems.

5 Conclusions

In this work, a hydrotalcite-derived NiFe catalyst was synthesized *via* co-precipitation and was partially reduced to produce a highly active and stable $Ni_9Fe_1/NiAlO_z$ catalyst. Using PPE as a lignin model, the $Ni_9Fe_1/NiAlO_z$ catalyst exhibited 99.4% PPE conversion with 56.8 and 40.5% yields of ethyl cyclohexane and cyclohexanol, respectively, under mild conditions of 100 °C and 0.8 MPa H_2. This catalyst exhibited high activity with actual EHL with a total yield of monomers 169.5 mg per g EHL at 300 °C and 3 MPa H_2. After recycling 6 times, 99.8% PPE conversion was still maintained.

The results of catalyst characterization and controlled catalytic *in situ* experiments further revealed the structure of the catalyst and the synergistic effect of active sites. After the reduction of the catalyst, the metal structure in the LDH changes. Although the EXAFS results indicate that the present form of metal in the catalyst is dominated by oxides, partial reduction of Ni in the catalyst yielded Ni_3Fe_1 alloy. However, the remaining Ni species existed as $NiAlO_z$, resulting in abundant OVs and a large surface area of about 325.7 $m^2\ g^{-1}$. The presence of an alloy phase is necessary, leading to the electron-rich phenomenon of Ni and stabilizing it, which is an important basis for the existence of high activity of the catalyst. Moreover, the presence of rich OVs further promotes the hydrogenation reaction steps. In the $Ni_9Fe_1/NiAlO_z$ catalyst, the synergistic effects of reactive metal species and OVs supported its excellent EHL depolymerization and hydrogenation activities. In this

work, a multi-active site synergistic high hydrogenation activity of a hydrotalcite-derived alloy catalyst strategy is established to decompose lignin into valuable monocyclic products with a high yield and provides new insights into the development of catalysts for abundant biomass conversion.

Data availability

The data that support the findings of this study are available from the corresponding author upon reasonable request.

Author contributions

Hairui Jiao performed the catalyst preparation, characterization studies and reaction tests and wrote the draft. Yushuai Sang facilitates further in-depth analysis of catalyst characterization results Hong Chen and Yongdan Li conceived the idea and revised the paper.

Conflicts of interest

The authors declare that they have no known competing financial interests or personal relationships that could have appeared to influence the work reported in this paper.

Acknowledgements

This work has received funding from the European Union's Horizon 2020 research and innovation program, (Building a low-carbon, climate resilient future: secure, clean and efficient energy) under Grant Agreement No. 101006744. The content presented in this document represents the views of the authors, and the European Commission has no liability in respect of the content. Dr Chen would like to express her gratitude to the National Natural Science Foundation of China (21690083 and 21808163).

References

1 Z. Cai, J. Long, Y. Li, L. Ye, B. Yin, L. J. France, J. Dong, L. Zheng, H. He, S. Liu, S. C. E. Tsang and X. Li, *Chem*, 2019, **5**, 2365–2377.
2 C. Zhang and F. Wang, *Acc. Chem. Res.*, 2020, **53**, 470–484.
3 X. Shen and R. Sun, *Carbohydr. Polym.*, 2021, **261**, 117884.
4 J. Bai, Y. Zhang, X. Zhang, C. Wang and L. Ma, *ACS Sustainable Chem. Eng.*, 2021, **9**, 7112–7119.
5 Y. Cao, G. Zhu, Y. Li, N. L. Breton, C. Gourlaouen, S. Choua, J. Boixel, H.-P. J. D. Rouville and J.-F. Soulé, *J. Am. Chem. Soc.*, 2022, **144**, 5902–5909.
6 M. Oregui-Bengoechea, I. Agirre, A. Iriondo, A. Lopez-Urionabarrene-chea, J. M. Requies, I. Agirrezabal-Telleria, K. Bizkarra, V. L. Barrio and J. F. Cambra, *Top. Curr. Chem.*, 2019, **377**, 36.
7 G. Xu, J. Guo, Y. Qu, Y. Zhang, Y. Fu and Q. Guo, *Green Chem.*, 2016, **18**, 5510–5517.
8 L. Dong, L. Lin, X. Han, X. Si, X. Liu, Y. Guo, F. Lu, S. Rudić, S. F. Parker, S. Yang and Y. Wang, *Chem*, 2019, **5**, 1521–1536.
9 D. Wu, Q. Wang, O. V. Safonova, D. V. Peron, W. Zhou, Z. Yan, M. Marinova, A. Y. Khodakov and V. V. Ordomsky, *Angew. Chem., Int. Ed.*, 2021, **60**, 12513–12523.
10 B. Chen, C. He, M. Cao, X. Qiu, X. Ouyang and Y. Qian, *Green Chem.*, 2022, **24**, 846–857.
11 F. Mauriello, E. Paone, R. Pietropaolo, A. M. Balu and R. Luque, *ACS Sustainable Chem. Eng.*, 2018, **6**, 9269–9276.
12 C. Chen, D. Wu, P. Liu, H. Xia, M. Zhou, X. Hou and J. Jiang, *React. Chem. Eng.*, 2021, **6**, 559–571.
13 Q. Han, M. U. Rehman, J. Wang, A. Rykov, O. Y. Gutierrez, Y. Zhao, S. Wang, X. Ma and J. A. Lercher, *Appl. Catal., B*, 2019, **253**, 348–358.
14 Z. Sun, G. Bottari, A. Afanasenko, M. C. A. Stuart, P. J. Deuss, B. Fridrich and K. Barta, *Nat. Catal.*, 2018, **1**, 82–92.
15 D. Yang, J. Huang, Z. Hu, F. Miao, Z. Zhang, Y. Xie, S. Liu, Q. Wang and C. U. Pittamn Jr, *Fuel*, 2024, **357**, 129982.
16 F. Yan, R. Ma, X. Ma, K. Cui, K. Wu, M. Chen and Y. Li, *Appl. Catal., B*, 2017, **202**, 305–313.
17 O. Hu, M. Lu, M. Cai, J. Liu, X. Qiu, C. Guo, C. Zhang and Y. Qian, *Adv. Mater.*, 2024, **36**, 2407129.
18 J. Shen, M. Cai, G. Li, C. Guo, X. Qiu and Y. Qian, *Adv. Funct. Mater.*, 2024, 2413597.
19 H. Duan, J. Dong, X. Gu, Y.-K. Peng, W. Chen, T. Issariyakul, W. K. Myers, M.-J. Li, N. Yi, A. F. R. Kilpatrick, Y. Wang, X. Zheng, S. Ji, Q. Wang, J. Feng, D. Chen, Y. Li, J. C. Buffet, H. Liu, S. C. Edman Tsang and D. O'Hare, *Nat. Commun.*, 2017, **8**, 591.
20 H. Zhou, M. Wang and F. Wang, *Joule*, 2021, **5**, 3031–3044.
21 L. Huang, F. Tang, P. Liu, W. Xiong, S. Jia, F. Hao, Y. Lv and H. Luo, *Fuel*, 2022, **327**, 125115.
22 T. Qin, Q. Lu, H. Xiang, X. Luo and S. Yuan, *Energy*, 2023, 128374.
23 G. S. Foo, A. K. Rogers, M. M. Yung and C. Sievers, *ACS Catal.*, 2016, **6**, 1292–1307.
24 L. Nie, P. M. de Souza, F. B. Noronha, W. An, T. Sooknoi and D. E. Resasco, *J. Mol. Catal. A: Chem.*, 2014, **388–389**, 47–55.
25 M. Chu, X. Wang, X. Wang, P. Xu, L. Zhang, S. Li, K. Feng, J. Zhong, L. Wang, Y. Li, L. He, M. Cao, Q. Zhang, L. Chi and J. Chen, *J. Am. Chem. Soc.*, 2024, **146**, 10655–10665.
26 X. Wang, Y. Tong, W. Feng, P. Liu, X. Li, Y. Cui, T. Cai, L. Zhao, Q. Xue, Z. Yan, X. Yuan and W. Xing, *Nat. Commun.*, 2023, **14**, 3767.
27 R. Insyani, M.-K. Kim, J.-W. Choi, C.-J. Yoo, D. J. Suh, H. Lee, C. S. Kim, K. H. Kim, K. Kim and J.-M. Ha, *Chem. Eng. J.*, 2022, **446**, 136578.
28 F. Liu, H. He and L. Xie, *ChemCatChem*, 2013, **5**, 3760–3769.
29 Y. Gao, Z. Zhao, H. Jia, X. Yang, X. Lei, X. Kong and F. Zhang, *J. Mater. Sci.*, 2019, **54**, 14515–14523.
30 H. Fang, J. Zheng, X. Luo, J. Du, A. Roldan, S. Leoni and Y. Yuan, *Appl. Catal., A*, 2017, **529**, 20–31.
31 Y. Zhai, C. Li, G. Xu, Y. Ma, X. Liu and Z. Ying, *Green Chem.*, 2017, **19**, 1859–1903.
32 Z. Liu, Y. Yu, Y. Liu, A. Ying, X. Zhang and Y. Wang, *ACS Catal.*, 2024, **14**, 2115–2126.
33 X. Yu, J. Chen and T. Ren, *RSC Adv.*, 2014, **4**, 46427–46436.

34 M. C. Biesinger, B. P. Payne, A. P. Grosvenor, L. W. M. Lau, A. R. Gerson and R. S. C. Smart, *Appl. Surf. Sci.*, 2011, **257**, 2717–2730.
35 Z. Tian, X. Liang, R. Li, C. Wang, J. Liu, L. Lei, R. Shu and Y. Chen, *Fuel*, 2022, **308**, 122034.
36 J. Bao, X. D. Zhang, B. Fan, J. Zhang, M. Zhou, W. Yang, X. Hu, H. Wang, B. Pan and Y. Xie, *Angew. Chem., Int. Ed.*, 2015, **54**, 7399–7404.
37 F. Cheng, T. Zhang, Y. Zhang, J. Du, X. Han and J. Chen, *Angew. Chem., Int. Ed.*, 2013, **52**, 2474–2477.
38 W. Liu, Y. Yang, L. Chen, E. Xu, J. Xu, S. Hong, X. Zhang and M. Wei, *Appl. Catal., B*, 2021, **282**, 119569.
39 X. Zhang, J. Wu, T. Li, C. Zhang, L. Zhu and S. Wang, *Chem. Eng. J.*, 2022, **429**, 132181.
40 Y. Ma, Y. Sang, K. Wu, Q. Liu, H. Chen and Y. Li, *Catal. Today*, 2023, **408**, 194–203.
41 Q. Hu, L. Yang, G. Fan and F. Li, *J. Catal.*, 2016, **340**, 184–195.
42 H. Jiao, G. Xu, Y. Sang, H. Chen and Y. Li, *Catal. Today*, 2024, **430**, 114542.
43 J. Song, Z. Huang, L. Pan, J. Zou, X. Zhang and L. Wang, *ACS Catal.*, 2015, **5**, 6594–6599.
44 J. Lu, J. Song, H. Niu, L. Pan, X. Zhang, L. Wang and J. Zou, *Appl. Surf. Sci.*, 2016, **371**, 61–66.